



Enhanced COD Reduction of Olefin Plant Spent Caustic Wastewater Using Easily Recyclable Cu(BDC)/MgO Nanocomposites

Soleiman Mosleh ^{a*} , Mohammad Mehdi Sabzehmeidani ^b

^a Polymer Eng. Dept., Faculty of Gas and Petroleum, Yasouj University, Gachsaran, Iran.

^b Chem. Eng. Dept., University of Science and Technology of Mazandaran, Behshahr, Iran.

ARTICLE INFO	ABSTRACT
<p>Article History: Received: 08 March 2025 Revised: 16 February 2026 Accepted: 12 April 2026 Published: 12 April 2026</p> <p>Article type: Research</p> <p>Keywords: Artificial Neural Network, Cu(BDC)/MgO Nanocomposites, Chemical Oxygen Demand Spent Caustic Degradation, Petrochemical Effluent</p>	<p>This study explored the photocatalytic degradation process for treating industrial spent caustic wastewater, focusing on reducing chemical oxygen demand (COD). Cu(BDC)/MgO nanocomposites were synthesized via microwave-assisted synthesis and served as efficient photocatalysts. An artificial neural network (ANN) model was developed to estimate COD concentrations and optimize treatment parameters, aiming to achieve superior COD reduction. The research aimed to minimize the hydrogen peroxide-to-COD ratio and to optimize other factors influencing COD removal. The synthesized nanocomposites were characterized by X-ray diffraction (XRD), field emission scanning electron microscopy (FE-SEM), and energy-dispersive X-ray spectroscopy (EDS) elemental mapping. Optimal parameters for achieving a 97.55% COD removal efficiency were identified as a nanocomposite dose of 1.30 g/L, an H₂O₂/Spent caustic wastewater ratio of 1.50 ml/L, a pH of 3.0, a treatment time of 35 min, and an aeration flow rate of 2.50 L/min. Catalyst recycling studies demonstrated the exceptional recyclability and stability of the Cu(BDC)/MgO nanocomposites, showing they could be reused as catalysts even after five treatment cycles. This highlights the potential for prolonged and sustainable use of these nanocomposites in wastewater treatment processes, effectively reducing COD levels in spent caustic effluents.</p>

Introduction

A large amount of organic wastewater is generated by industrial activities, especially petroleum and refinery operations, which contain persistent pollutants [1, 2]. Spent caustic, a complex and hazardous wastewater from gas scrubbing and petrochemical processes, is difficult to treat due to its high pollutant content, highly alkaline conditions (pH > 12), elevated salinity (5-12 wt% sodium), and a high sulfide content (2-3 wt%) [3, 4]. Effective management and pre-treatment of spent caustic are crucial before conventional wastewater treatment can be applied [5]. Olefin units in the oil and gas industry use caustic substances, particularly sodium hydroxide, to remove organic sulfur compounds, hydrogen sulfide, carbon dioxide, acidic components, and other impurities from hydrocarbon streams such as natural gas and liquid petroleum gas [6, 7]. Caustic is also used to treat furnace exhaust gases, absorb CO₂, purify petroleum cuts, dehydrate hydrocarbons, and in processes like gas washing and oil sweetening [8, 9]. Additionally, it is applied for scrubbing gasoline, kerosene, and distilled oils. However, the resulting spent caustic is a hazardous, toxic industrial effluent with high alkalinity, an unpleasant odor, and high concentrations of sulfide ions and volatile organic compounds [10,

* Corresponding Authors: S. Mosleh (E-mail address: mosleh@yu.ac.ir)



11]. These properties limit available treatment options, making conventional methods such as open-air, biological, and Fenton technologies less effective [12]. Strict environmental policies further complicate the design of the treatment system.

Treatment methods for spent caustic are mainly categorized as biological, chemical, and thermal processes, each with drawbacks related to efficiency, cost, safety, and secondary pollution risks [13, 14]. Chemical treatments, especially chemical oxidation, are the most widely used and can be divided into classical and advanced oxidation processes (AOPs). These AOPs comprise various techniques, including Fenton oxidation, electrochemical oxidation, photo-Fenton oxidation, UV-based processes, sonolysis, nonthermal plasmas, photocatalysis, and radiolysis methods [15]. Photocatalytic degradation stands out for effectively degrading hazardous, refractory organic pollutants, thanks to its strong oxidation capacity and environmental compatibility [16]. However, its large-scale application is limited by rapid charge-carrier recombination [17]. A two-step process of acid neutralization and steam stripping is used to treat spent caustic, reducing but not fully eliminating mercaptans and sulfides, which can still cause odors [18]. The effluent retains high BOD and COD due to persistent organic compounds, and the feedstock composition in olefin plants influences sulfur content and COD control [19, 20]. Due to these limitations, photocatalytic degradation is proposed as a more effective method for COD removal. Conventional photocatalysts have limited efficiency due to their small surface areas and dependence on UV light, which results from their large band gaps [21]. To address these issues, new photocatalyst materials that can be activated by visible light are being explored to improve efficiency and applicability [22]. The properties of nanomaterials are closely linked to their geometric structures, making the study of structure-property relationships crucial [23]. Various nano-metal oxides, such as magnesium oxide, have attracted attention for their unique properties [24, 25]. Combining different metal oxides enables property customization, with MgO standing out for its non-toxicity, cost-effectiveness, and reusability [26-29]. Although several methods can synthesize nano-MgO, its photocatalytic efficiency is limited by the poor light harvesting and fast charge recombination [30-33]. Current research focuses on defect engineering, carbon composites, morphology control, and transition-metal doping to enhance sunlight-driven activity [34-38]. The present study aims to synthesize a novel Cu(BDC)/MgO nanocomposite for efficient photocatalytic degradation of COD in petrochemical wastewater. In Cu(BDC) MOFs, photon-absorbing organic linkers generate charge-separated states, but photocatalytic efficiency is limited by electron-hole recombination [39]. Integrating MgO with Cu(BDC) reduces this recombination, enhancing performance. Copper is preferred for MOF synthesis due to its low cost, abundance, and non-toxicity, with Cu-BDC (from copper nitrate and terephthalic acid) offering easy, eco-friendly preparation [40, 41]. Cu-BDC shows high stability in aqueous solutions across a wide pH range, due to strong coordination bonding between copper and the -COOH groups of BDC [42, 43]. In this work, the microwave-assisted synthesis was employed for its rapid, energy-efficient, and safe reaction conditions. To elucidate the complex, nonlinear behavior of the photocatalytic system, an ANN was utilized, offering time and cost advantages over traditional experimental designs.

Experimental Section

Chemicals and Instruments

All chemicals and solvents used in this study were procured from Sigma-Aldrich and were of analytical grade, employed as received without further purification. For pH measurement, an AL20 pH/Redox/Temperature meter (AQUALYTIC, Germany) was used. COD was measured

using the LCK 014 kit (HACH company). XRD analysis was performed using a Philips instrument (model: PW 1800) with Cu α radiation (40 kV and 40 mA). The morphology of the synthesized nanocomposites was examined using a FE-SEM (Sigma, Zeiss), while EDS tests were performed through a silicon drift detector from Oxford Instruments.

Synthesis Procedure

Cu(BDC)/MgO nanocomposites were synthesized via microwave-assisted synthesis [44]. Initially, a mixture of copper (II) nitrate trihydrate (1.45 g) and terephthalic acid (1 g) was combined with 75 mL of DMF and stirred at 25 °C for 10 min. The solution was then subjected to ultrasonic treatment for 1 minute to ensure complete dissolution. The resulting solution was then transferred to a microwave oven and heated at 700 W for 8 min. The blue precipitate formed was filtered and washed with fresh DMF three times. Finally, the obtained Cu-BDC MOF was oven-dried at 220 °C for 24 h.

The nano-sized magnesium oxide (MgO) powder was prepared by precipitation [45]. The aqueous magnesium nitrate hydroxide solution was prepared by dissolving 0.02 mol of $\text{Mg}(\text{NO}_3)_2 \cdot 6\text{H}_2\text{O}$ in 100 mL of double-distilled water. The mixture was stirred for 4 h until it became transparent. To adjust the pH to 9, ammonia was added dropwise to the solution. This resulted in the immediate formation of a precipitate. The resulting precipitate was washed repeatedly with methanol and distilled water, subsequently filtered and dried overnight in an oven maintained at 100 °C. After grinding, the dried material was calcined at 500 °C for 3 hours in a muffle furnace, yielding the final MgO nanopowder. To prepare Cu(BDC)/MgO nanocomposites, 0.5 g of the as-prepared MgO nano-powder was dispersed in a solution containing 1.45 g of copper (II) nitrate trihydrate and 1 g of terephthalic acid. After the combination with 75 mL of DMF, the mixture was stirred at a fixed temperature for 15 min. Afterward, the solution was subjected to an ultrasonic bath for 1 min to facilitate complete dissolution. Next, the solution was heated in a microwave oven at 700 W for 5 min. The resulting solid precipitate was then centrifuged, washed three times with distilled water, and dried at 220 °C in an oven for 24 h. Fig. 1 depicts a schematic representation of the synthesis process.



Fig. 1. Schematic of the synthesis procedure

Treatment Process

To assess the photocatalytic capabilities of Cu(BDC)/MgO nanocomposites, this photocatalyst was used to reduce COD in spent caustic wastewater. The optimal conditions for maximum COD removal were identified experimentally. The effects of various operational factors were examined in this investigation, including photocatalyst loading (g/L), H₂O₂/SCW

(ml/L), H_2O_2 concentration (g/L), pH, operation time (min), and aeration rate (L/min). To conduct the tests, a 2000 cm^3 photocatalytic reactor (Fig. 2) was used. A mechanical stirrer was included to facilitate mixing. An air pump equipped with a sparger was used to guarantee sufficient oxygen transfer. The reaction temperature was controlled by coolant water recirculation through the jacket of the photocatalytic reactor. For each run, the solution volume of 1500 cm^3 was adjusted to the desired pH using $0.1\text{ M H}_2\text{SO}_4$ and 0.1 M NaOH . The resulting solution was then introduced into the photocatalytic reactor. Subsequently, the stirring was initiated, and a specific quantity of Cu(BDC)/MgO nanocomposites was added to attain the required concentration. To achieve maximum adsorption of the nanocomposites at equilibrium, the mixture was stirred for 20 min before activating the lamps. Once the lamps were turned on, both the lamps and the aeration system were activated. Following the designated reaction period, the samples were promptly collected and transferred into a flask. Sodium hydroxide solution was subsequently introduced to halt the reaction and eliminate any remaining hydrogen peroxide that could interfere with COD analysis. The samples were centrifuged at 4500 rpm for 5 min and filtered before measuring COD. COD analysis is widely utilized as a reliable method for quantifying the organic content present in wastewater. This technique assesses waste by determining the total oxygen required to oxidize organic substances to carbon dioxide and water. In this study, COD levels were measured using HACH's COD procedure with the aid of a COD reactor. The standard closed reflux and colorimetric techniques were applied, and sample absorbance for the COD assessment was determined using a spectrophotometer [46]. The efficiency of COD removal was calculated according to Eq. 1:

$$\text{COD Removal (\%)} = (\text{COD}_0 - \text{COD}_t / \text{COD}_0) \times 100 \quad (1)$$

where COD_0 corresponds to the chemical oxygen demand at the initial time, and COD_t represents the value measured at time t . To eliminate interference from residual H_2O_2 and terminate the reaction, a sodium hydroxide solution was introduced.

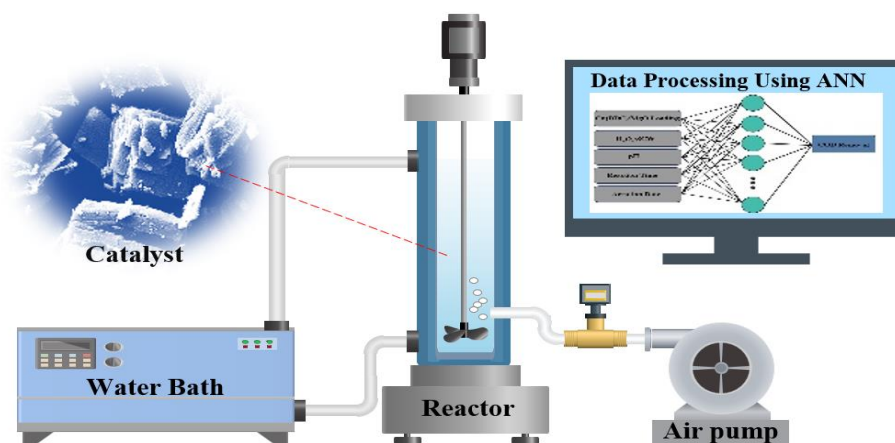


Fig. 2. Schematic of reactor set-up

The raw effluent characteristics (Table 1) were collected from the neutralization stage of the Olefin unit and used as the input wastewater sample for the photocatalytic reactor.

Table 1. The key characteristics of the wastewater used

Characteristic	Measurement unit	Amount
COD	mg/L	1360
TDS	mg/L	285
Na ₂ S	wt %	0.5
pH	-	12.70
Na ₂ CO ₃	wt %	2.5
NaOH	wt %	3
Phenols	mg/L	420

Process Modeling Utilizing Artificial Neural Network (ANN)

The evaluation of process performance used ANN modeling to assess the impact of five major factors. These factors include photocatalyst loading, pH, H₂O₂/SCW, reaction time, and aeration rate. Table 2 presents the range and levels of the operational parameters.

Table 2. Range and level of main operational parameters

Parameter	Unit	Range
Photocatalyst dosage	g/L	0.25-2.50
H ₂ O ₂ /SCW	ml/L	1.0-3.0
pH	-	2.0-12
Aeration rate	L/min	0.5-5.0
Reaction time	min	10-60

In the present study, experimental data were used to train an established ANN model composed of input, hidden, and output layers. Fig. 3 illustrates the network structure based on the selected input variables. To evaluate the performance of the artificial neural network, Eqs 2-5 were used to calculate the adjusted R-squared (R^2), Mean Absolute Error (MAE), Absolute Average Deviation (AAD), and Root Mean Squared Error (RMSE).

$$R_{adj}^2 = 1 - \left[(1 - R^2) \frac{n - 1}{n - K - 1} \right] \quad (2)$$

$$RMSE = \sqrt{\frac{\sum_{i=1}^n (X_{im} - X_{ip})^2}{n}} \quad (3)$$

$$MAE = \frac{\sum_{i=1}^n |X_{im} - X_{ip}|}{n} \quad (4)$$

$$AAD = \left\{ \frac{\sum_{i=1}^n |X_{im} - X_{ip}| / X_{im}}{n} \right\} \times 100 \quad (5)$$

where K represents the number of input variables, and n represents the number of data points. X_{im} and X_{ip} are the predicted and actual values, respectively, for the response variable.

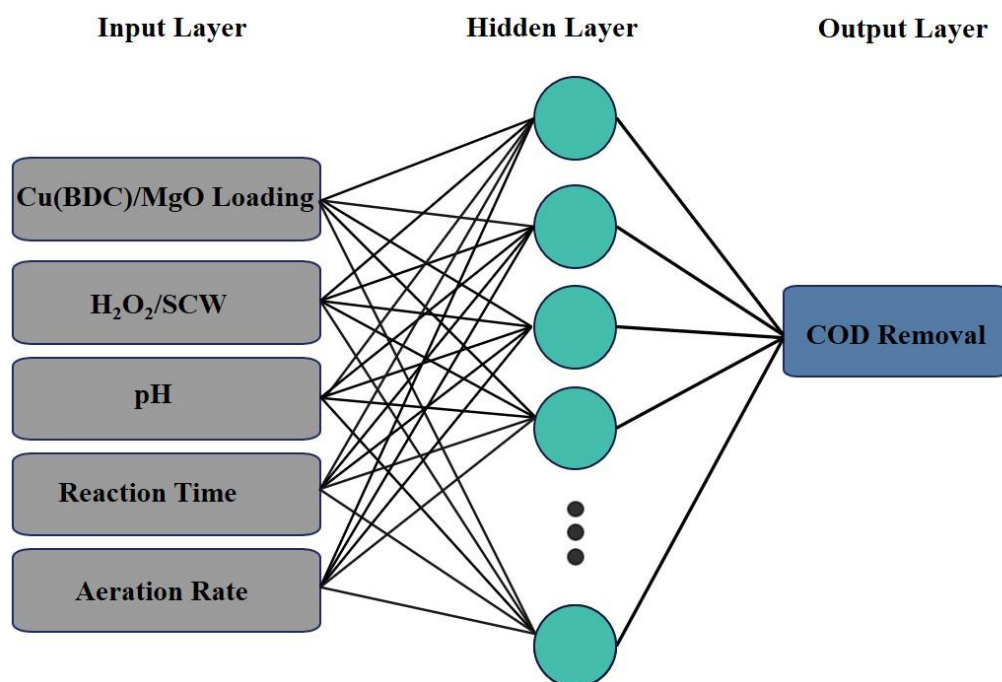


Fig. 3. Structure of the applied neural network for process modeling

Quality Assurance of the Data

To ensure the results presented were reproducible and reliable, all procedures were performed in triplicate. Furthermore, COD analysis was conducted in triplicate for each sample, with a relative standard deviation (RSD) of less than 2%. This additional step enhanced the reliability of the findings.

Results and Discussion

Structure and Composition of the Prepared Nanocomposites

Fig. 4 illustrates pronounced peaks with robust intensity for the Cu-BDC sample (XRD pattern). These peaks exhibit a remarkable resemblance to patterns reported in the literature, thereby providing additional confirmation of the successful synthesis of Cu-BDC [47, 48]. The Cu(BDC) compound can be identified by its characteristic peaks at various angles (2θ) in the X-ray diffraction pattern. As indicated in Fig. 4, the distinctive peaks of the synthesized Cu-BDC (CCDC no. 687690) are located at $2\theta = 9.9^\circ, 12.0^\circ, 13.5^\circ, 17.1^\circ, 20.4^\circ, 24.9^\circ, 34.1^\circ,$ and 42.2° . In Fig. 4, the pattern of MgO nanoparticles is also presented. The peaks located at 2θ values of $36.9^\circ, 42.9^\circ, 62.3^\circ, 74.6^\circ,$ and 78.6° within the 2θ range can be attributed to the (1 1 1), (2 0 0), (220), (311), and (222) planes, respectively, of the structured MgO nanopowders. The absence of any additional peaks shows the high purity of the prepared MgO nanoparticles.

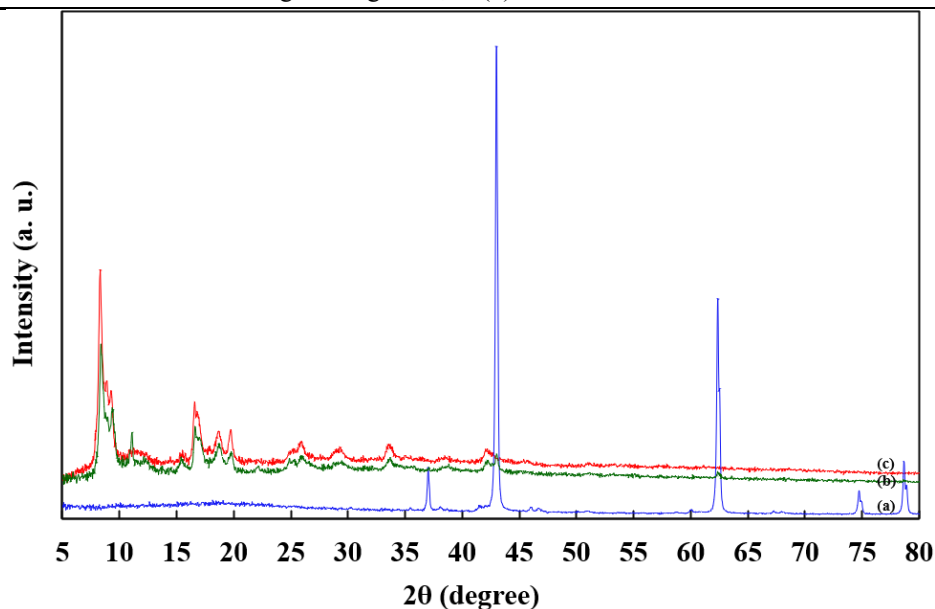
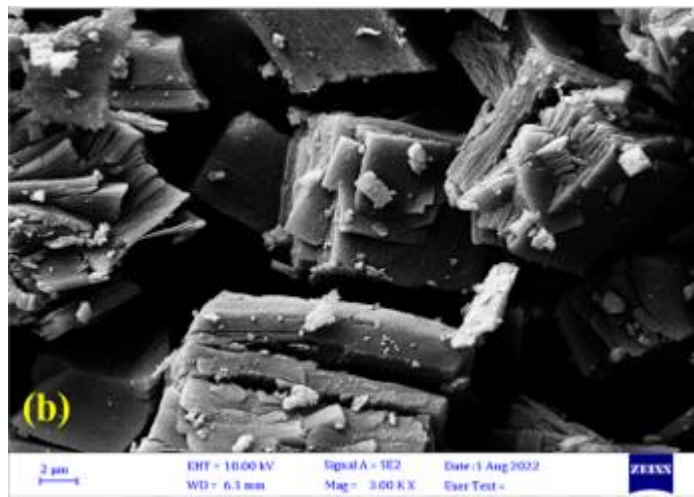
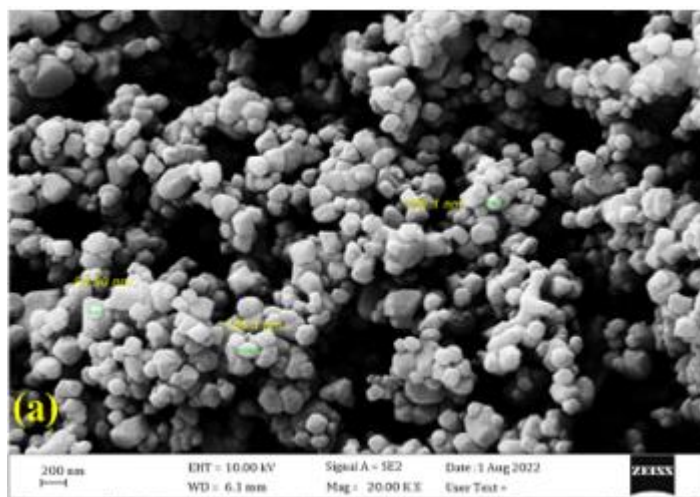


Fig. 4. XRD pattern of samples. (a) MgO nanoparticles, (b) Cu(BDC) MOF, and (c) Cu(BDC)/MgO nanocomposites

The SEM images presented in [Fig. 5](#) illustrate the as-synthesized samples. The SEM image shows that the Cu-BDC MOF exhibits a uniform morphology, with well-formed cubic shapes. These observations align with the XRD patterns, further confirming the agreement between the MOF's morphology and crystal structure. In [Fig. 5a](#), a representative SEM image of the synthesized MgO nanoparticles is displayed. Upon examination of these SEM images, it becomes evident that the nanoparticles form assemblies, each composed of round nanoparticles.



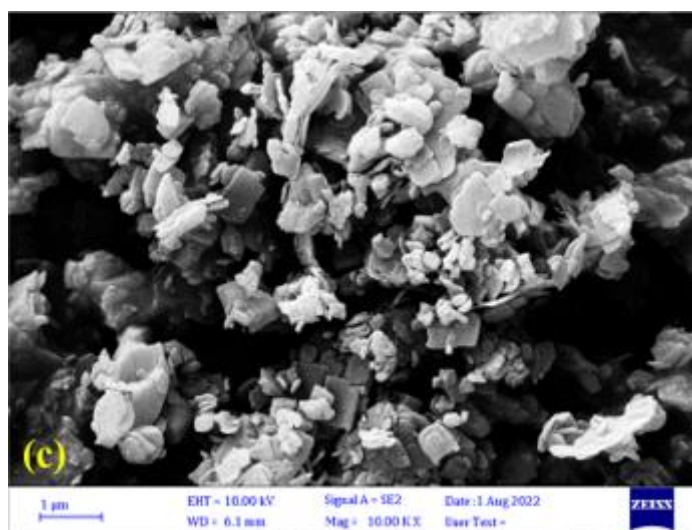


Fig. 5. FE-SEM images. (a) MgO nanoparticles, (b) Cu(BDC) MOF , and (c) Cu(BDC)/MgO nanocomposites

In the [Figs. 6a-c](#), the EDS analyses of the materials are compared. Findings indicate that the as-prepared composite contains atoms characteristic of Cu(BDC), as expected. However, in addition to these atoms, the presence of Mg atoms is also observed. The detection of C, Cu, and O atoms can be ascribed to the Cu-BDC MOF components in the structure of the Cu(BDC)/MgO nanocomposites. The observation of Mg atoms further confirms the stabilization of MgO nanoparticles on the Cu(BDC)/MgO nanocomposites. In the [Figs. 6d-f](#), the elemental mapping analysis of the Cu(BDC)/MgO nanocomposites is presented. The results demonstrate that the MgO nanoparticles exhibit a high dispersion throughout the sample, indicating that the MgO nanoparticles have been uniformly stabilized on the Cu(BDC)/MgO nanocomposites. This observation suggests that the synthesis method employed has successfully achieved a uniform distribution of MgO nanoparticles within the Cu(BDC)/MgO nanocomposites.

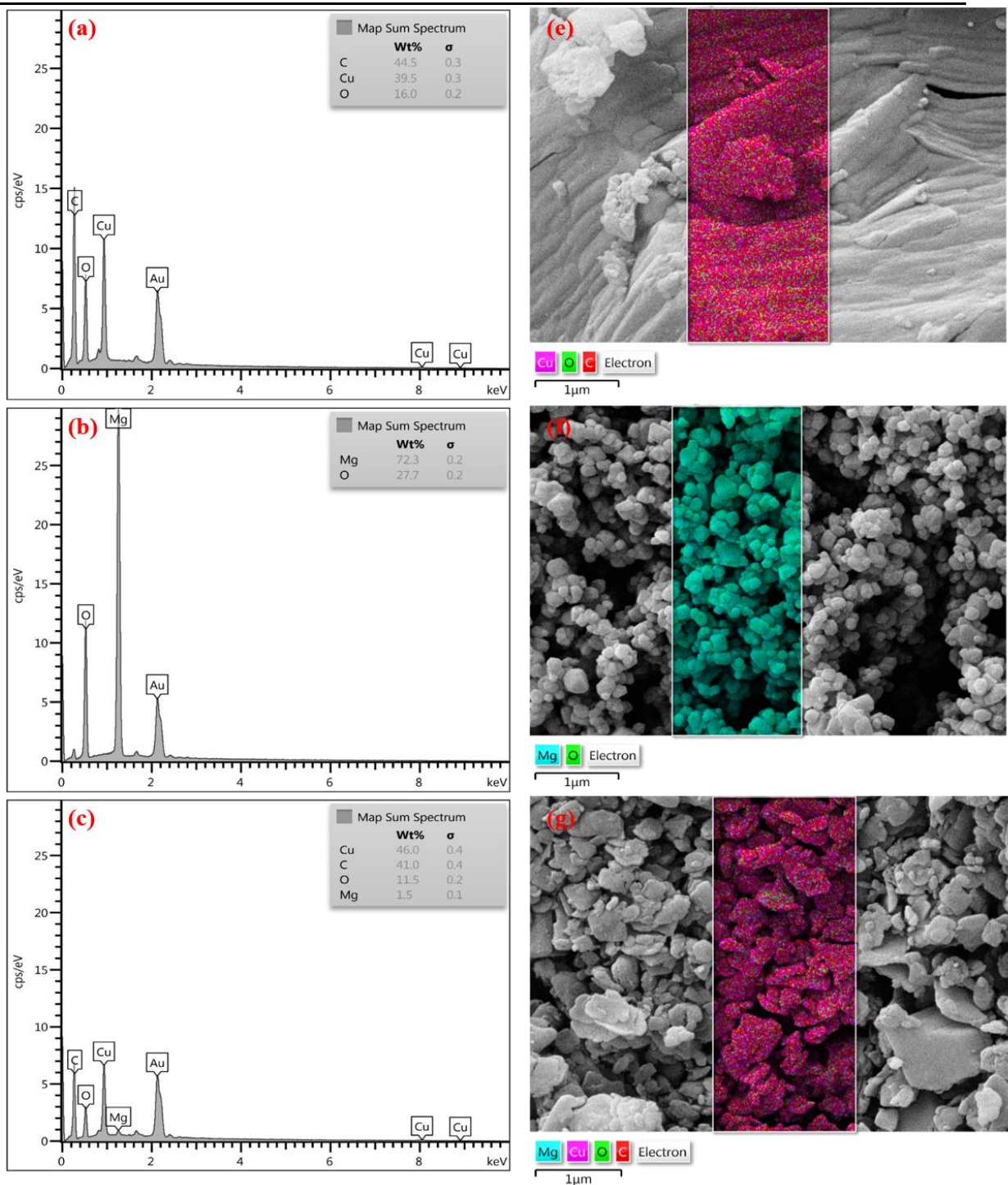


Fig. 6. EDS analysis for (a) Cu(BDC) MOF, (b) MgO nanoparticles, (c) Cu(BDC)/MgO nanocomposites. Elemental mapping analysis for (d) Cu(BDC) MOF, (e) MgO nanoparticles, and (f) Cu(BDC)/MgO nanocomposites

N_2 physisorption analysis was applied to evaluate the textural properties (i.e., surface area and porosity) of the Cu(BDC) MOF, MgO nanoparticles, and Cu(BDC)/MgO nanocomposite. The surface area-to-volume ratio plays a crucial role in the adsorption properties of the prepared nanocomposite. Cu(BDC)/MgO nanocomposites follow a Type III isotherm, as per the Brunauer-DeMing-DeMing-Teller classification. As shown in Fig. 7a, the total pore volume of Cu(BDC) MOF, MgO nanoparticles, and Cu(BDC)/MgO samples is equal to 0.184, 0.095, and 0.277 cm^3g^{-1} the total surface area of Cu(BDC) MOF, MgO nanoparticles, and Cu(BDC)/MgO samples is 22.9, 13.3, and 189.8 m^2g^{-1} (Fig. 7b).

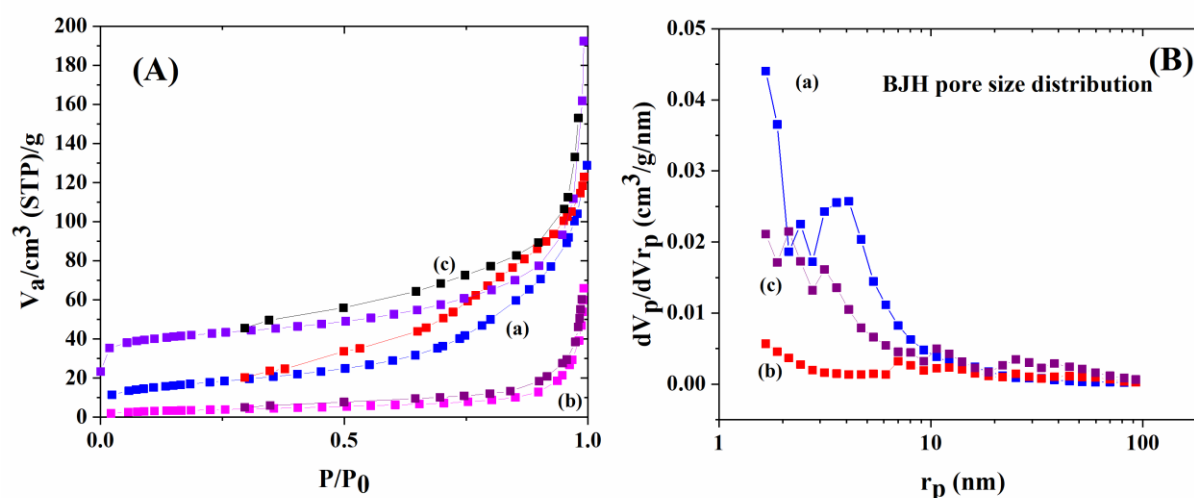


Fig. 7. (a) Nitrogen adsorption-desorption isotherms, and (b) the corresponding pore size distributions of the prepared samples

The Effects of Operational Parameters on COD Reduction

To assess the photocatalytic degradation capabilities of Cu(BDC)/MgO nanocomposites, the catalyst was used to reduce chemical oxygen demand (COD) in spent caustic wastewater. The study systematically examined the effects of five variables, including pH, nanocomposite dosage (g/L), aeration rate (L/min), time (min), and H₂O₂/wastewater ratio (ml/L), on reduction efficiency. Among these, pH plays a crucial role in photocatalytic reactions. Typically, such processes are more effective under acidic conditions. When the pH increases at low oxidant concentrations, a decline in process efficiency is observed, suggesting an inverse relationship between pH and oxidant levels. Additionally, raising the photocatalyst concentration often requires a corresponding increase in pH to prevent particle aggregation.

The interaction of photogenerated holes with H₂O molecules or OH⁻ mainly facilitates the formation of hydroxyl radicals[•]. When other sources for hydroxyl radical production (e.g., hydroperoxyl radicals) are insufficient, enhancing the photocatalyst dosage can compensate for this deficiency. However, under alkaline conditions, the adsorption of contaminants onto the catalyst surface diminishes, thereby lowering the degradation rate. Investigating the effect of pH over 2.0 to 12 revealed that optimal COD reduction occurs at pH 3.0 (Fig. 8a).

The impact of photocatalyst dosage was also explored (Fig. 8b). Increasing the photocatalyst dosage increases the number of active sites available for electron-hole pair generation. These sites facilitate the formation of free electrons, which reduce molecular oxygen to superoxide radicals (O₂^{-•}). The positive holes oxidize H₂O to produce hydroxyl radicals (•OH). As highly reactive oxidants, hydroxyl radicals can mineralize even persistent organic pollutants. Therefore, increasing the catalyst concentration enhances free radical production, thereby accelerating oxidation reactions and improving COD reduction efficiency.

In AOPs, H₂O₂ serves as a strong oxidant. Higher concentrations of hydrogen peroxide result in more molecules per unit volume, and under irradiation with a photocatalyst, it decomposes to form additional hydroxyl radicals. The elevated levels of these radicals further promote the oxidation of various organic contaminants in wastewater, resulting in more rapid reductions in COD (Fig. 8c).

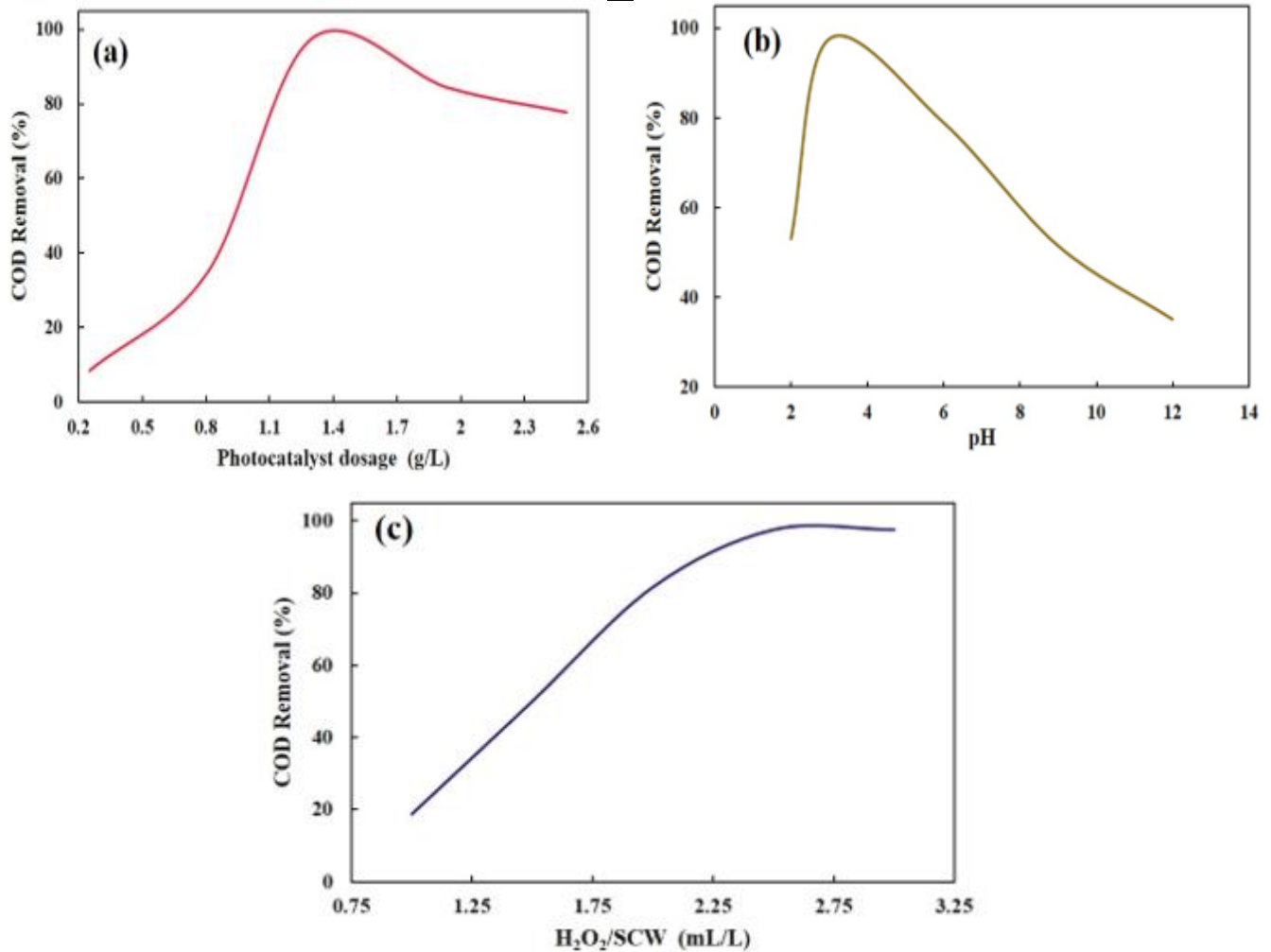


Fig. 8. The effects of operational parameters on COD reduction. (a) pH, (b) photocatalyst loading (g/l), and (c) H₂O₂/SCW

The study also highlights the importance of optimizing aeration rates as a significant factor in designing and operating advanced oxidation water treatment systems (Fig. 9a). Enhanced aeration improves mixing and facilitates better mass transfer between oxygen and catalyst particles, thereby increasing free radical generation and resulting in greater COD reduction in treated effluent.

Furthermore, data indicate that extending irradiation time in photocatalytic processes directly boosts the removal efficiency of organic pollutants. Longer exposure allows more photons to reach the catalyst surface, generating additional electron-hole pairs that can participate in oxidation reactions with contaminants (Fig. 9b). This increase in both direct and indirect oxidation events with prolonged irradiation ultimately leads to improved pollutant removal outcomes. Collectively, these findings offer valuable insights for developing more efficient and cost-effective wastewater treatment technologies based on advanced oxidation processes.

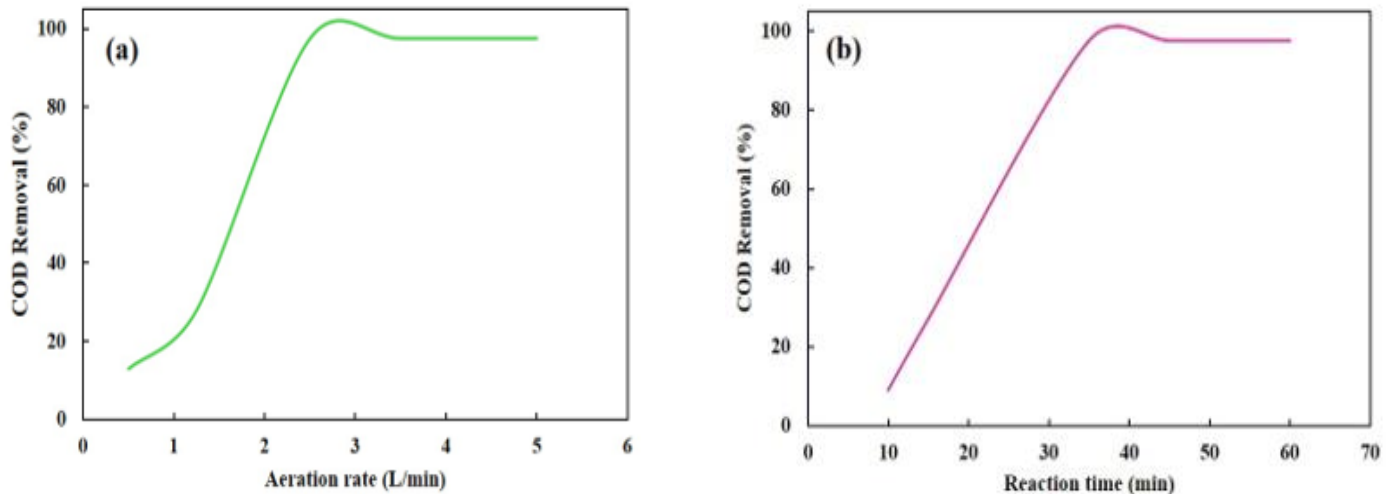
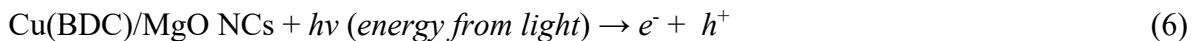


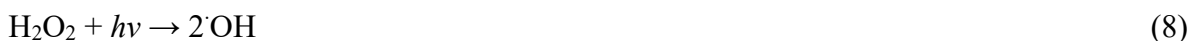
Fig. 9. The effects of operational parameters on COD reduction: (a) aeration rate (L/min), and (b) Reaction time (min)

Degradation Mechanism

Photocatalytic processes primarily proceed through two main mechanisms. The first involves the use of hydroxyl or water groups on the photocatalyst surface, while the second mechanism entails direct oxidation within the catalyst's cavities. When Cu(BDC)/MgO nanocomposites are exposed to light, electron-hole pairs are generated on the catalyst surface. The resulting holes associate with H₂O or hydroxyl groups, forming hydroxyl radicals that degrade organic pollutants. The sequence of reactions can be described as follows:



The photogenerated electrons reduce oxygen molecules to form superoxide and hydroperoxide radical anions, which subsequently convert into hydrogen peroxide and water. Hydrogen peroxide can further undergo photolysis to yield additional hydroxyl radicals:



The elimination of sulfides is attributed both to their thermal decomposition at elevated temperatures and to their direct reaction with hydrogen peroxide, as represented by the following equations:



The breakdown of hydrogen peroxide may release oxygen, which can further facilitate the oxidation of sulfides. During this process, sulphidic intermediates such as thiosulphates, sulfites, and sulfates may form. Additionally, phenolic intermediates, including hydroquinone, p-benzoquinone, and catechol, have been detected at lower concentrations than organic acids [49].

The photocatalytic method is effective for degrading organic contaminants. In this investigation, 82.10% reduction in phenolic substances and 97.55% reduction in COD of wastewater were achieved. Additionally, a 4.5% decrease in sulfide compounds was observed, likely due to adsorption of these pollutants onto the catalyst surface. Inorganic ions, including Na^+ originating from Na_2S , Na_2CO_3 , and NaOH , remain mostly unchanged since they do not undergo oxidation. The total dissolved solids (TDS) exhibit minimal decrease—generally less than 10%—because the treatment primarily targets organic compounds rather than inorganic salts.

The Process of Modeling and Optimizing Using ANN

To identify the most favorable experimental conditions using the ANN model, 26 experiments were conducted using a systematic experimental design developed after selecting suitable intervals for the independent variables. The investigated parameters comprised photocatalyst concentration (0.25–2.50 g/L), $\text{H}_2\text{O}_2/\text{SCW}$ ratio (1.0–3.0 ml/L), pH level (2.0–12), aeration rate (0.5–5.0 L/min), and reaction duration (10–60 min). The ANN-based process model was constructed using the Single Layer Perceptron (SLP) architecture. The SLP network consisted of five input nodes, representing the loading of the photocatalyst, $\text{H}_2\text{O}_2/\text{SCW}$, pH, reaction time, and aeration rate. Additionally, there was a single output node indicating the COD removal achieved during the process. To train the network, a feedforward approach was used, in which an input training pattern was passed through the network. In a feedforward neural network, each neuron in a layer is connected to all neurons in the adjacent layer. The training process used the Trainbr function, which updates weights and biases using the Levenberg-Marquardt (LM) optimization algorithm. LM minimizes a joint function of squared errors and weights, aiming to find the optimal solution that enables the network to generalize well. This approach is known as Bayesian regularization. In this study, various numbers of neurons were examined in the ANN's hidden layer. The optimal number of neurons was determined by evaluating the correlation coefficient and the minimum Mean Squared Error (MSE) across the entire dataset. Fig. 10 illustrates the results. To ensure the reliability of the results, three separate runs were conducted for each network structure. Each run used different random values for the neural network's initial weights. This approach helps to account for any potential bias or variability introduced by the initial weight values.

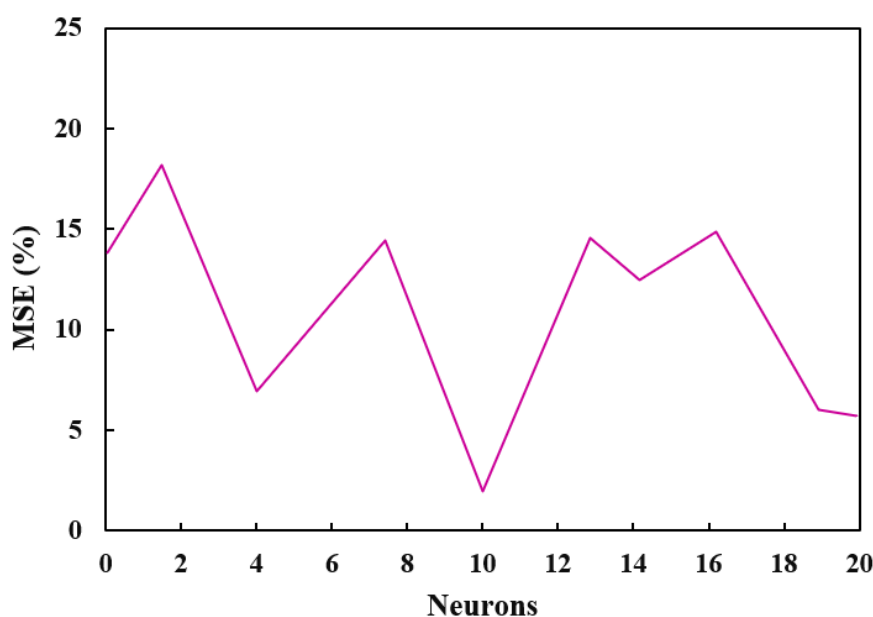


Fig. 10. The relation between MSE (%) and the number of neurons in the hidden layer

Table 3 presents the statistical values of the ANN model, including correlation coefficients, AAD, RMS, and MAE. A good model is characterized by R^2 being close to 1.0 and in good agreement with R^2_{adj} . A high R^2 value indicates a strong linear relationship. RMS should be close to zero, indicating the good agreement between the ANN model estimates and the experimental values. A small AAD between the observed and predicted values indicates a high degree of correlation between the model's estimations and the actual data. Higher values of AAD and RMS indicate larger estimation errors. It is worth noting that in the ANN model, large values of R^2 and R^2_{adj} , along with small differences between them, indicate the model's accuracy in predicting the desired outcome.

Model factor	Value
R^2	0.9912
R^2_{adj}	0.9983
AAD	0.2966
MAE	0.2095
RMS	0.2240

Catalytic Stability

The practical application of a catalyst relies significantly on its recyclability and stability. The stability of the photocatalyst was assessed through cycling experiments that evaluated its performance after multiple photocatalytic degradation cycles. **Fig. 11** demonstrates that even after 6 cycles of photocatalytic COD removal in caustic petrochemical wastewater, the Cu(BDC)/MgO nanocomposite sample exhibited remarkable stability, maintaining an 86% removal rate.

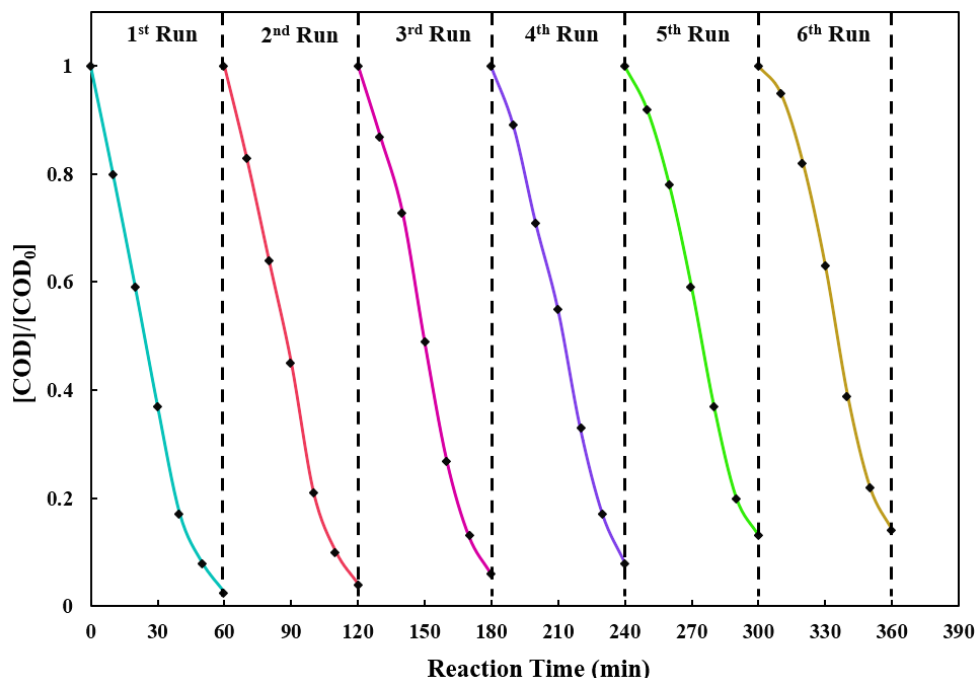


Fig. 11. Reusability of Cu(BDC)/MgO nanocomposites toward photocatalytic degradation of SCW

Comparison of the Activity of Cu(BDC)/MgO Nanocomposites with Some Reported Catalysts

The COD reduction performance of the developed system was compared with literature values, as shown in Table 4. The results in the table demonstrate that the proposed system effectively promotes COD reduction with the least time requirement.

Table 4. Comparison of the performance of different treatment systems

System/process	Time (min)	COD removal (%)
Photocatalytic degradation [18]	90	77.3%
Membrane system [42]	480	93.71%
Neutralization [5]	60	88%
Fenton process [5]	60	96.5%
Electro-photo-Fenton [43]	80	97%
This work	35	97.55%

Conclusion

In summary, the Cu(BDC)/MgO nanocomposites were prepared via microwave-assisted synthesis. The materials were characterized by XRD, FE-SEM, EDS, and elemental mapping techniques to analyze their structural, morphological, and elemental properties. The ANN-based models for predicting COD concentrations in spent caustic effluent were developed by applying a three-layered ANN to assess wastewater treatment performance. The fabricated nanocomposites exhibited high photocatalytic activity in reducing the COD of spent caustic. The optimal conditions for achieving the maximum COD removal (97.55%) were determined to be a photocatalyst loading of 1.30 g/L, H₂O₂/SCW of 1.50 ml/L, pH of 3.0, time of 35 min, and an aeration rate of 2.50 L/min. Furthermore, a remarkable degree of concordance was observed between the experimental data and the ANN model's values at the optimized conditions.

Nomenclature

AAD	Absolute Average Deviation
ANN	Artificial neural network
AOPs	Advanced Oxidation Processes
BET	Brunauer-Emmett-Teller
BOD	Biological Oxygen Demand
COD	Chemical Oxygen Demand
DRS	Diffuse Reflectance Spectroscopy
EDX	Energy Dispersive X- Ray
FE- SEM	Field Emission Scanning Electron Microscopy
FTIR	Fourier Transform Infrared Spectroscopy
LM	Levenberg-Marquardt
MAE	Mean Absolute Error
MgO	Magnesium Oxide
MSE	Mean Squared Error
RMSE	Root Mean Squared Error
RSD	Relative Standard Deviation
SCW	Spent Caustic Wastewater
SLP	Single Layer Perceptron
WAO	Wet Air Oxidation
WWTF	Wastewater Treatment Facility
XRD	X-Ray Diffraction

Declaration of Competing Interest

The authors affirm that they have no known competing financial interests or personal relationships that could have potentially influenced the work presented in this paper.

Acknowledgment

The authors express their gratitude to the Research Council of Yasouj University for providing financial support for this research. The authors also extend their appreciation to the Gachsaran Petrochemical Complex (Olefin Plant) for their valuable cooperation in facilitating this project.

References

- [1] Liu J, Jiang L, Zhang H, Yao H, Chai J, Wang J, Fang D, Zhang Z, Tie M. Construction of high-proportion dual bismuth-based Z-scheme $\text{Bi}_3\text{O}_4\text{Cl}/\text{Bi}_2\text{MoO}_6$ photocatalytic system via in-situ growth of Bi_2MoO_6 on $\text{Bi}_3\text{O}_4\text{Cl}$ for enhanced photocatalytic degradation of organic pollutants. *Journal of Alloys and Compounds*. 2023 Sep 15;956:170375. <https://doi.org/10.1016/j.jallcom.2023.170375>
- [2] Li J, Wang Q, Liang J, Li H, Guo S, El-Din MG, Chen C. Enhanced disintegration using refinery spent caustic for anaerobic digestion of refinery waste-activated sludge. *Journal of Environmental Management*. 2021 Apr 15;284:112022. <https://doi.org/10.1016/j.jenvman.2021.112022>
- [3] Delnavaz M, Khoshvaght H, Sadeghi A, Ghasemipannah K, Aliabadi MH. Experimental, statistical, and financial analysis of the treatment of organic contaminants in naphthenic spent caustic soda using the electrocoagulation process modified by carbon nanotubes. *Journal of Cleaner Production*. 2021 Dec 10;327:129515. <https://doi.org/10.1016/j.jclepro.2021.129515>
- [4] Hashemi SR, Heydarinasab A, Amoozegar MA. Modified biological treatment of spent caustic effluent from liquefied petroleum gas plants. *Chemical Engineering & Technology*. 2020 Feb;43(2):380-5. <https://doi.org/10.1002/ceat.201900368>
- [5] Hawari A, Ramadan H, Abu-Reesh I, Ouederni M. A comparative study of the treatment of ethylene plant spent caustic by neutralization and classical and advanced oxidation. *Journal of environmental management*. 2015 Mar 15;151:105-12. <https://doi.org/10.1016/j.jenvman.2014.12.038>
- [6] Zhang X, Liu T, Zhang Y, Cai Z, Wan Q. Co-operative harmless treatment and neutralization utilization process research of LPG spent caustic coupled chloroaluminate ionic liquid spent catalysts. *Journal of Water Process Engineering*. 2023 Apr 1;52:103507. <https://doi.org/10.1016/j.jwpe.2023.103507>
- [7] Alipour Z, Azari A. COD removal from industrial spent caustic wastewater: A review. *Journal of environmental chemical engineering*. 2020 Jun 1;8(3):103678. <https://doi.org/10.1016/j.jece.2020.103678>
- [8] González C, Pariente MI, Molina R, Espina LG, Masa MO, Bernal V, Melero JA, Martínez F. Increasing biodegradability of a real amine-contaminated spent caustic problematic stream through WAO and CWAO oxidation using a high specific surface catalyst from petcoke. *Chemical Engineering Journal*. 2023 Mar 15;460:141692. <https://doi.org/10.1016/j.cej.2023.141692>
- [9] Ntagia E, Fiset E, Hong LT, Vaiopoulou E, Rabaey K. Electrochemical treatment of industrial sulfidic spent caustic streams for sulfide removal and caustic recovery. *Journal of Hazardous Materials*. 2020 Apr 15;388:121770. <https://doi.org/10.1016/j.jhazmat.2019.121770>

- [10] Rita AI, Rodrigues CS, Santos M, Sanches S, Madeira LM. Comparison of different strategies to treat challenging refinery spent caustic effluents. Separation and purification technology. 2020 Dec 15;253:117482. <https://doi.org/10.1016/j.seppur.2020.117482>
- [11] Fernandes A, Makoś P, Wang Z, Boczkaj G. Synergistic effect of TiO₂ photocatalytic advanced oxidation processes in the treatment of refinery effluents. Chemical Engineering Journal. 2020 Jul 1;391:123488. <https://doi.org/10.1016/j.cej.2019.123488>
- [12] Gholami A, Mousavi SB, Heris SZ, Mohammadpourfard M. Highly efficient treatment of petrochemical spent caustic effluent via electro-Fenton process for COD and TOC removal: optimization and experimental. Biomass Conversion and Biorefinery. 2024 Aug;14(15):17481-97. <https://doi.org/10.1007/s13399-023-03772-2>
- [13] Davarnejad R, Bakhshandeh M. Olefin plant spent caustic wastewater treatment using electro-Fenton technique. Egyptian journal of petroleum. 2018 Dec 1;27(4):573-81. <https://doi.org/10.1016/j.ejpe.2017.08.008>
- [14] Dong C, Fang W, Yi Q, Zhang J. A comprehensive review on reactive oxygen species (ROS) in advanced oxidation processes (AOPs). Chemosphere. 2022 Dec 1;308:136205. <https://doi.org/10.1016/j.chemosphere.2022.136205>
- [15] Hua X, Chen H, Rong C, Addison F, Dong D, Qu J, Liang D, Guo Z, Zheng N, Liu H. Visible-light-driven photocatalytic degradation of tetracycline hydrochloride by Z-scheme Ag₃PO₄/1T@ 2H-MoS₂ heterojunction: degradation mechanism, toxicity assessment, and potential applications. Journal of Hazardous Materials. 2023 Apr 15;448:130951. <https://doi.org/10.1016/j.jhazmat.2023.130951>
- [16] Zhao Y, Chang L, Li Y, He W, Liu K, Cui M, Hameed MU, Xie J. High-gravity photocatalytic degradation of tetracycline hydrochloride under simulated sunlight. Journal of Water Process Engineering. 2023 Jul 1;53:103753. <https://doi.org/10.1016/j.jwpe.2023.103753>
- [17] Wei Y, Zhao J, Liu Z, Zhang L, Cui Q, Wang H. Study on wet oxidation process and mechanism for ethylene spent caustic. Environmental Technology. 2022 Jul 29;43(17):2637-46. <https://doi.org/10.1080/09593330.2021.1892200>
- [18] Ahmadpour A, Asl AH, Fallah N. Synthesis and photocatalytic studies of TiO₂-clinoptilolite on spent caustic wastewater treatment. Particulate Science and Technology. 2018 Oct 3;36(7):791-8. <https://doi.org/10.1080/02726351.2017.1302534>
- [19] Sarkodie B, Amesimeku J, Frimpong C, Howard EK, Feng Q, Xu Z. Photocatalytic degradation of dyes by novel electrospun nanofibers: a review. Chemosphere. 2023 Feb 1;313:137654. <https://doi.org/10.1016/j.chemosphere.2022.137654>
- [20] Xu P, Ding C, Li Z, Yu R, Cui H, Gao S. Photocatalytic degradation of air pollutant by modified nano titanium oxide (TiO₂) in a fluidized bed photoreactor: Optimizing and kinetic modeling. Chemosphere. 2023 Apr 1;319:137995. <https://doi.org/10.1016/j.chemosphere.2023.137995>
- [21] AlSalhi MS, Devanesan S, Asemi NN, Aldawsari M. Construction of SnO₂/CuO/rGO nanocomposites for photocatalytic degradation of organic pollutants and antibacterial applications. Environmental Research. 2023 Apr 1;222:115370. <https://doi.org/10.1016/j.envres.2023.115370>
- [22] Fouda A, Hassan SE, Saied E, Hamza MF. Photocatalytic degradation of real textile and tannery effluent using biosynthesized magnesium oxide nanoparticles (MgO-NPs), heavy metal adsorption, phytotoxicity, and antimicrobial activity. Journal of Environmental Chemical Engineering. 2021 Aug 1;9(4):105346. <https://doi.org/10.1016/j.jece.2021.105346>
- [23] Zhu Z, Xia H, Li H. Boosting photocatalytic degradation efficiency of tetracycline by a visible-light-activated NiMoO₄/g-C₃N₄ heterojunction photocatalyst in the water environment. Solid State Sciences. 2023 May 1;139:107164. <https://doi.org/10.1016/j.solidstatesciences.2023.107164>
- [24] Chandrasekar M, Subash M, Perumal V, Panimalar S, Aravindan S, Uthrakumar R, Inmozhi C, Isaev AB, Muniyasamy S, Raja A, Kaviyarasu K. Specific charge separation of Sn doped MgO nanoparticles for photocatalytic activity under UV light irradiation. Separation and Purification Technology. 2022 Aug 1;294:121189. <https://doi.org/10.1016/j.seppur.2022.121189>



- [25] Scott T, Zhao H, Deng W, Feng X, Li Y. Photocatalytic degradation of phenol in water under simulated sunlight by an ultrathin MgO coated Ag/TiO₂ nanocomposite. *Chemosphere*. 2019 Feb 1;216:1-8. <https://doi.org/10.1016/j.chemosphere.2018.10.083>
- [26] Prabhu PS, Kathirvel P, Maruthamani D, Ram SG. Enhanced photocatalytic activity of methylene blue dye by DIFS synthesized pure and Mn doped MgO nanostructures. *Optik*. 2023 Jul 1;283:170869. <https://doi.org/10.1016/j.ijleo.2023.170869>
- [27] Zheng X, Gou Y, Peng H, Mao Y, Wen J. Nonthermal plasma sulfurized CuInS₂/S-doped MgO nanosheets for efficient solar-light photocatalytic degradation of tetracycline. *Colloids and Surfaces A: Physicochemical and Engineering Aspects*. 2021 Sep 20;625:126900. <https://doi.org/10.1016/j.colsurfa.2021.126900>
- [28] Ratnam MV, Karthikeyan C, Rao KN, Meena V. Magnesium oxide nanoparticles for effective photocatalytic degradation of methyl red dye in aqueous solutions: optimization studies using response surface methodology. *Materials Today: Proceedings*. 2020 Jan 1;26:2308-13. <https://doi.org/10.1016/j.matpr.2020.02.498>
- [29] Chahar D, Kumar D, Thakur P, Thakur A. Visible light induced photocatalytic degradation of methylene blue dye by using Mg doped Co-Zn nanoferrites. *Materials Research Bulletin*. 2023 Jun 1;162:112205. <https://doi.org/10.1016/j.materresbull.2023.112205>
- [30] Ali AA, El Fadaly EA, Deraz NM. Auto-combustion fabrication, structural, morphological and photocatalytic activity of CuO/ZnO/MgO nanocomposites. *Materials Chemistry and Physics*. 2021 Sep 15;270:124762. <https://doi.org/10.1016/j.matchemphys.2021.124762>
- [31] An X, Chen Y, Ao M, Jin Y, Zhan L, Yu B, Wu Z, Jiang P. Sequential photocatalytic degradation of organophosphorus pesticides and recovery of orthophosphate by biochar/ α -Fe₂O₃/MgO composite: A new enhanced strategy for reducing the impacts of organophosphorus from wastewater. *Chemical Engineering Journal*. 2022 May 1;435:135087. <https://doi.org/10.1016/j.ccej.2022.135087>
- [32] Su X, Cao N, Feng J, Li W, Ding X, Li Z, Gao M, Hu L, Zhang H, Ren Y, Wei T. The enhanced photocatalytic performance of the amorphous carbon/MgO nanofibers: Insight into the role of the oxygen vacancies and 1D morphology. *Applied Surface Science*. 2023 Apr 15;616:156470. <https://doi.org/10.1016/j.apsusc.2023.156470>
- [33] Mylarappa M, Raghavendra N, Surendra BS, Kumar KS, Kantharjau S. Electrochemical, photocatalytic and sensor studies of clay/MgO nanoparticles. *Applied Surface Science Advances*. 2022 Aug 1;10:100268. <https://doi.org/10.1016/j.apsadv.2022.100268>
- [34] Bateni A, Valizadeh K, Salahshour Y, Behroozi AH, Maleki A. Fabrication and characterization of pectin-graphene oxide-magnesium ferrite-zinc oxide nanocomposite for photocatalytic degradation of diclofenac in an aqueous solution under visible light irradiation. *Journal of Environmental Management*. 2022 Dec 15;324:116358. <https://doi.org/10.1016/j.jenvman.2022.116358>
- [35] Liu Y, Zhang L, Liu T, Wang J. Photocatalytic selective oxidation of ammonium to dinitrogen by FeO_x-MgO activated persulfate under solar-light irradiation. *Chemical Engineering Journal*. 2023 Feb 15;454:140499. <https://doi.org/10.1016/j.ccej.2022.140499>
- [36] Arif S, Nawaz M, Siddique S, Ayub R, Saleem S. Synthesis, characterization and photocatalytic activity of Mg_{1-x}Cu_xO nanoparticles for wastewater treatment. *Materials Today Communications*. 2022 Dec 1;33:104361. <https://doi.org/10.1016/j.mtcomm.2022.104361>
- [37] Abdollahi B, Farshnama S, Asl EA, Najafidoust A, Sarani M. Cu (BDC) metal-organic framework (MOF)-based Ag₂CrO₄ heterostructure with enhanced solar-light degradation of organic dyes. *Inorganic Chemistry Communications*. 2022 Apr 1;138:109236. <https://doi.org/10.1016/j.inoche.2022.109236>
- [38] Sadjadi S, Koohestani F. Palladated composite of Cu-BDC MOF and perlite as an efficient catalyst for hydrogenation of nitroarenes. *Journal of Molecular Structure*. 2022 Feb 15;1250:131793. <https://doi.org/10.1016/j.molstruc.2021.131793>
- [39] Silva BC, Irikura K, Flor JB, Dos Santos RM, Lachgar A, Frem RC, Zanoni MV. Electrochemical preparation of Cu/Cu₂O-Cu (BDC) metal-organic framework electrodes

- for photoelectrocatalytic reduction of CO₂. *Journal of CO₂ Utilization*. 2020 Dec 1;42:101299. <https://doi.org/10.1016/j.jcou.2020.101299>
- [40] Alamgholiloo H, Zhang S, Ahadi A, Rostamnia S, Banaei R, Li Z, Liu X, Shokouhimehr M. Synthesis of bimetallic 4-PySI-Pd@ Cu (BDC) via open metal site Cu-MOF: Effect of metal and support of Pd@ Cu-MOFs in H₂ generation from formic acid. *Molecular Catalysis*. 2019 Apr 1;467:30-7. <https://doi.org/10.1016/j.mcat.2019.01.031>
- [41] Sadjadi S, Koohestani F. Composite of magnetic carbon quantum dot-supported ionic liquid and Cu-BDC (CCDC no. 687690) MOF: A triple catalytic composite for chemical transformations. *Journal of Solid State Chemistry*. 2022 Apr 1;308:122888. <https://doi.org/10.1016/j.jssc.2022.122888>
- [42] Zhao L, Xia W. Stainless steel membrane UF coupled with NF process for the recovery of sodium hydroxide from alkaline wastewater in chitin processing. *Desalination*. 2009 Dec 15;249(2):774-80. <https://doi.org/10.1016/j.desal.2009.01.036>
- [43] Nasr Esfahani K, Farhadian M, Solaimany Nazar AR. Interaction effects of various reaction parameters on the treatment of sulfidic spent caustic through electro-photo-Fenton. *International Journal of Environmental Science and Technology*. 2019 Nov;16:7165-74. <https://doi.org/10.1007/s13762-018-2126-8>
- [44] Mosleh S, Khaksar H. Cu-BDC MOF/CNFs hybrids for rapid CO₂ capture in a circulating fluidized bed via temperature swing adsorption process. *Chemical Engineering Science*. 2024 Apr 5;287:119773. <https://doi.org/10.1016/j.ces.2024.119773>
- [45] Hasan IF, Basim HS, Ibrahim RK, Saadoon NM, Saadoon MM. Effect of MgO-NPs on the Morphology and Function of Kidney in Male Albino Mice. *Journal of Nanostructures*. 2025 Oct 1;15(4):1690-9. <https://doi.org/10.22052/JNS.2025.04.016>
- [46] American Public Health Association. APHA standard methods for the examination of water and wastewater. Standard methods for the examination of water & wastewater. Washington, DC: American Public Health Association. 2005.
- [47] Sadjadi S, Koohestani F. Palladated composite of Cu-BDC MOF and perlite as an efficient catalyst for hydrogenation of nitroarenes. *Journal of Molecular Structure*. 2022 Feb 15;1250:131793. <https://doi.org/10.1016/j.molstruc.2021.131793>
- [48] Li Z, Xia H, Li S, Pang J, Zhu W, Jiang Y. In situ hybridization of enzymes and their metal-organic framework analogues with enhanced activity and stability by biomimetic mineralisation. *Nanoscale*. 2017;9(40):15298-302. <https://doi.org/10.1039/C7NR06315F>
- [49] James MS, Garg A. Performance of electro-Fenton process for the treatment of synthetic sulphidic spent caustic waste stream generated from petroleum refineries. *Chemosphere*. 2024 Jan 1;346:140572. <https://doi.org/10.1016/j.chemosphere.2023.140572>

How to cite: Mosleh S, Sabzehmeidani M.M. Enhanced COD Reduction of Olefin Plant Spent Caustic Wastewater Using Easily Recyclable Cu(BDC)/MgO Nanocomposites. *Journal of Chemical and Petroleum Engineering* 2026; 60(1): 89-107.